Exploring the nontrivial band edge in the bulk of the topological insulators Bi_2Se_3 and Bi_2Te_3

Robin Guehne [1,2,*] and Vojtěch Chlan [3]

[1] *Max Planck Institute for Chemical Physics of Solids, 01187 Dresden, Germany*

[2] *Felix Bloch Institute for Solid State Physics, Leipzig University, Linnéstraße 5, 04103 Leipzig, Germany*

[3] *Faculty of Mathematics and Physics, Charles University, V Holešovičkách 2, 180 00, Prague 8, Czech Republic*

(Received 31 August 2023; accepted 6 February 2024; published 28 February 2024)

Bi_2Se_3 and related compounds are prototype three-dimensional topological insulators with a single Dirac cone in the surface band structure. While the topological surface states can be characterized with surface-sensitive methods, the underlying bulk energy band inversion has not been investigated in detail. Here, a study is presented that combines density-functional theory and nuclear magnetic resonance to explore the nontrivial band edge of Bi_2Se_3 and Bi_2Te_3. It is found that the topological band inversion is not a discrete reversal of the order of the valence and conduction band at the Γ point. Rather, the bands closest to the Fermi level become well mixed and spread evenly below and above the band gap, such that the characters of the valence- and conduction-band edges become indistinguishable. Beside those bands relevant for the band inversion, i.e., Bi and Se p_z, also Bi p_x and p_y states are involved. As a part of this mixture of states, the band inversion shows no edges in k space.

DOI: 10.1103/PhysRevResearch.6.013214

I. INTRODUCTION

For more then a decade, the relevance of topologically nontrivial states of matter irresistibly grows into most fields of condensed matter science [1] and even beyond [2], rendering the topological approach for electronic band structures a cornucopia of fundamental concepts, including superconductivity and Majorana states, as well as the prospect of breakthrough applications in the area of spintronics and quantum computing. The exploration of topological systems is driven by vast theoretical effort to identify exotic band structures and related effects, as well as to advise how corresponding material properties and special electronic states can be experimentally characterized.

A key feature of topology is the Dirac cone, the linear dispersion characteristic for the honeycomb lattice of graphene hosting massless Dirac fermions [3]. Bi_2Se_3 and related compounds are prototypical three-dimensional topological insulators (TIs) that possess a Dirac cone in their surface electronic band structure allowing dissipation-free two-dimensional charge and spin transport [4]. The Dirac cone originates from a bulk energy band inversion that reverses the order of bonding (Se p_z) and antibonding states (Bi p_z) at the Fermi level. While the corresponding Dirac cone can be detected, e.g., with angle-resolved photoemission spectroscopy [5,6], the underlying bulk band inversion is much more difficult to probe.

A powerful method to investigate the bulk properties of a material is nuclear magnetic resonance (NMR) as it allows access to chemical as well as electronic properties with atomic resolution. For a number of materials, it has been shown that NMR can trace topology-related bulk features through the NMR shift and spin-lattice relaxation [7–12]. The potential of NMR in this field, however, is by far not exhausted, also because shift and relaxation phenomena are not well understood for strongly spin-orbit coupled systems, or difficult to calculate with *ab initio* methods, which obscures their significance. Still rarer, the electric quadrupole interaction (EQI) which is experienced by nuclei with spin $I > 1/2$ in noncubic environments is employed to study the electronic structure of quantum matter. With the EQI the *real*-space charge symmetry of a nucleus' surrounding can be explored with high precision, which is also easily calculated with first principles, allowing in principle a direct access to local inhomogeneities, phenomena related to bond covalency and charge disproportionality, or charge density waves.

In case of Bi_2Se_3 and Bi_2Te_3, the EQI of ^{209}Bi nuclei can be used to explore the real-space charge re-distribution induced by spin-orbit coupling (SOC), including the topological band inversion. The concept is shown in Fig. 1. The two panels confront the two cases of location of the charge at the Fermi edge without [Fig. 1(a)] and with SOC and band inversion [Fig. 1(b)]. Due to the small effective mass of the itinerant electrons in this system, self-doping through native defects yields a shift of the Fermi level into the valence/conduction band (depending on the type of defect). The corresponding carriers populate those bands that are involved in the band inversion. The states associated with these bands can be identified with density-functional theory (DFT)—the basis to predict Bi_2Se_3 and related compounds to be topological

*robin.guehne@cpfs.mpg.de

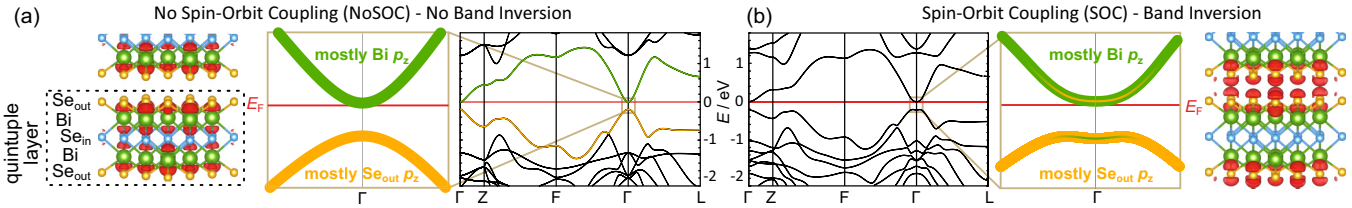

FIG. 1. The two cases of Bi_2Se_3 without (a) and with band inversion (b) induced by SOC are confronted. In the center the band structures are shown with schematic closeups of the Fermi edges to the respective left and right. The character of the bands involved in the band inversion, i.e., Bi (green) and Se_{out} (orange), defines the location of Fermi-level states (red) in the crystal structure. The calculations reveal, in agreement with NMR experiments, that the band inversion is embedded in a mixture of states below and above the Fermi level. In particular, the relevant conduction band states (Bi p_z) are partially moved to the valence band (and vice versa for Se_{out} p_z) as illustrated in the closeup Fermi edge in panel (b).

insulators [4]—and thus, the real-space location of these states in the crystal structure. In other words, SOC redistributes charge carriers between different crystal sites in real space, where the topological band inversion is given by a transfer between Bi and Se p_z states, and with NMR and the EQI, this redistribution can be measured quantitatively. And indeed, preliminary results from DFT computing the two cases of the trivial (NoSOC) and the nontrivial (SOC) band structure for Bi_2Se_3 reveal a sizable difference for the corresponding EQI, while the experimental value agrees well with the nontrivial case [13]. This finding establishes a completely new perspective onto the bulk band structure properties of topological insulators and allows for a detailed study of the nontrivial band edge in Bi_2Se_3.

In this paper, the results of such a detailed analysis for Bi_2Se_3 and Bi_2Te_3 are reported, including the comparison to experimental results. Using DFT calculations, the Bi electric-field gradient (EFG—representing the local charge symmetry) is explored down to 25 eV below the Fermi level to separate contributions of deeper bands from those involved in the band inversion. The local EFG at Bi sites is easily extracted from the calculations as it is determined by the local wave functions. Since the topological band inversion changes the wave functions of the valence and conduction bands, the character of the band inversion is imprinted in the local EFG, which in turn is measurable with Bi NMR. The study shows how a real-space probe like NMR can be used to draw conclusions about k-space properties of a material. It is found that the band inversion is not a discrete shift of states from above the Fermi level to the valence band and vice versa, but rather, the band inversion is embedded in a mixture of states chiefly associated with Se_{out} p_z and Bi p_z as well as $p_{x/y} = p_x + p_y$ (due to symmetry, p_x and p_y are equivalent) bands. Hereby, all the states involved, including the topologically relevant Bi and Se p_z, are distributed evenly below and above the band gap, such that the Fermi edge character of the valence and the conduction band becomes indistinguishable. Thus, the topological band inversion has no edges in k space.

II. RESULTS AND DISCUSSION

In Fig. 2, the density of states (DOS) from −25 eV below the Fermi level up to 5 eV above is shown, for NoSOC (grey), SOC (red), and their difference (green). In addition, the corresponding EFGs for isolated DOS bunches are provided below. The reason for the bunch-wise treatment is that the EFG can only be calculated for a complete band, sometimes spreading over several eV. Note, spin-orbit coupling is fully calculated inside the atomic spheres for noncore states and can only be switched on/off (for core states the SOC and all relevant relativistic contributions are always included in the calculations).

For the lowermost energies in Fig. 2, a splitting of the bands associated with Bi $5d$ states into $5d^{3/2}$ and $5d^{5/2}$ states due to SOC is observed. The corresponding EFGs do not change measurably, as expected for closed shells. The two bunches between about −14 and −12 eV, and −11 and −7 eV also do not show a significant effect on the EFG, once SOC is switched on. Most likely, because these states can predominately be assigned to the character of Bi $6s$ and Se $4s$ that do not give rise to an EFG for symmetry reasons. A large contribution of the Bi EFG stems from bands closest to the Fermi level (−5 to 0 eV). These bands consist mostly of Bi and Se p states, which dominate the chemical bonds [14]. The difference between the NoSOC and the SOC case is substantial, but with only a minor contribution (less than

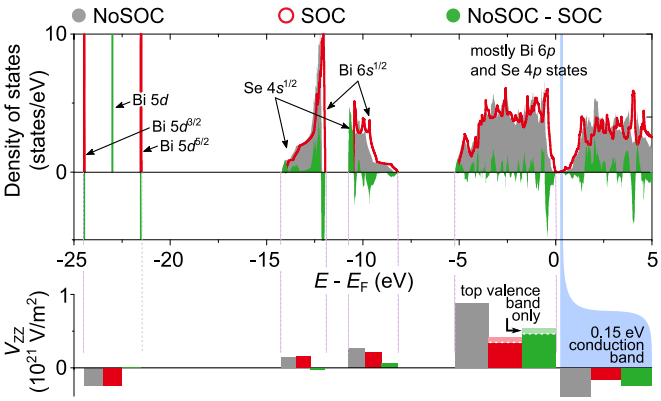

FIG. 2. DOS without (grey) and with (red) SOC, as well as their difference (green) from −25 to 5 eV. Below, the corresponding EFGs for a given bunch of bands are shown. The small EFG arising from the top valence band [orange in Fig. 1(b)] is highlighted for the bunch of valence bands closest to the Fermi level (between −5 and 0 eV). The narrow blue slice covers the first 150 meV of the conduction band, representing occupied states due to the Fermi-level shift as a consequence of doping 0.005 extra electrons per formula unit (concentration of free carriers of $\sim 4 \times 10^{19}$ cm^{-3}).

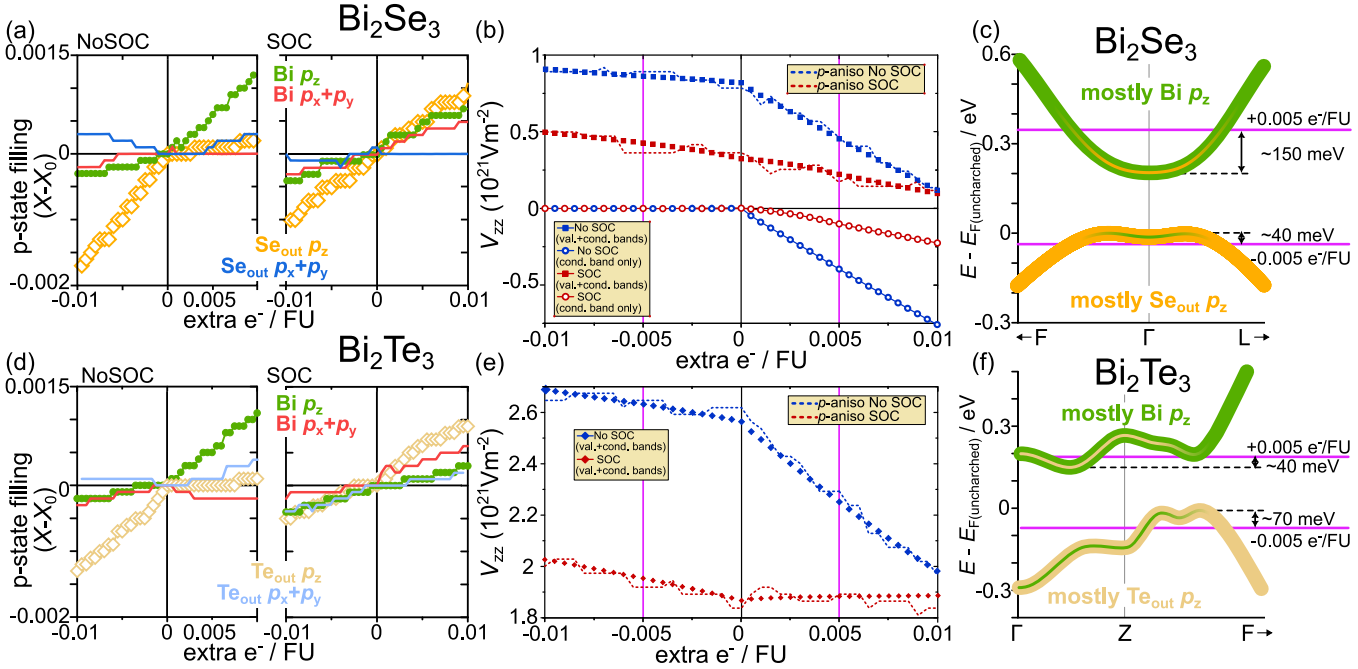

FIG. 3. Panels (a) and (d) depict the p-state occupancy for the two cases NoSOC and SOC upon doping Bi_2Se_3 and Bi_2Te_3, respectively, represented in extra charge per formula unit (extra charge of -1 $(+1)$ then means doping 1 hole (electron) per formula unit). The corresponding EFGs as a function of doping are shown in panels (b) and (e). Solid squares (diamonds) represent the total V_{ZZ}, including all valence and conduction bands, while open circles denote the V_{ZZ} as stemming from the lowermost conduction band only (zero for hole doping). Dashed lines denote Bi p-states population anisotropy, which connects state occupation and EFG. In the panels (c) and (f) close ups of the band edges of Bi_2Se_3 and Bi_2Te_3 with SOC are shown, including the position of the Fermi level (pink solid lines) for the doping cases of ± 0.005 e^-/FU. Note the different paths in the Brillouin zone, i.e., along the F $\rightarrow$ Γ $\rightarrow$ L (Bi_2Se_3) and the Γ $\rightarrow$ Z $\rightarrow$ F (Bi_2Te_3) direction (see text for details).

15%) originating from the top valence band (orange in Fig. 1). This finding emphasizes that the effect of the band inversion on the EFG of the valence band as a whole is obscured by deeper states, and thus, cannot be taken as an experimentally accessible signature.

The small change in the EFG, however, that arises in the top valence band once SOC is switched on, stems from Bi states that are brought from the conduction into the valence band due to the band inversion. If such small changes are reflected in the EFG, the band inversion could be sensed by investigating the evolution of the EFG with electron doping, which moves the Fermi level successively from the top valence band across the band gap into the lowermost conduction band. Any changes in the local EFG must then stem from the states participating in the band inversion. This is shown by the very narrow slice given in blue in Fig. 2, which represents the case of doping with 0.005 extra electrons per formula unit, shifting the Fermi level by about 150 meV into the conduction band. The corresponding EFGs are surprisingly large given the tiny energy range.

From the real-space point of view, the EFG is derived from the total charge density, comprising onsite effects as related to local orbitals, and offsite contributions that reflect the surrounding lattice. Typically the former dominate the EFG. Moreover, a small amount of electron or hole doping as considered in the present work, leaves the lattice unaffected, and thus, any observed changes in the EFG must reflect onsite effects. In WIEN2k the elements of the EFG tensor are evaluated directly from the calculated charge density [15], e.g., $V_{ZZ} \propto \int \frac{\varrho(\mathbf{r})Y_2^0}{r^3} d\mathbf{r}$. The charge density $\varrho(\mathbf{r})$ can be decomposed into different angular momentum contributions, and since in our case only the p states are relevant to EFG, the V_{ZZ} is mostly given by the p-p contribution. Therefore, in a good approximation (e.g., the radial part $\int \frac{1}{r^3} d\mathbf{r}$ does not change notably), the EFG follows the p-states population anisotropy [16] given by $p_{\text{aniso}} = 0.5 \times (p_x + p_y) - p_z$. This allows us to conveniently connect the Bi EFG values with the populations of the Bi p states as well as to understand how the EFG of Bi changes upon doping.

Individual orbital occupations for both, Bi_2Se_3 and Bi_2Te_3, their anisotropy, and the corresponding EFGs as a function of doping for the two cases NoSOC and SOC, as well as close-ups of the band structures for SOC are comprised in Fig. 3. In case of NoSOC, a very small charging around the Fermi level (negative for holes, positive for electrons) clearly determines the character of the valence (conduction) band to be chiefly given by Se_{out} p_z (Bi p_z) states. While the Bi EFG [Fig. 3, panel (b), blue symbols] is almost unaffected for hole doping, there is a visible bend of the EFG dependence at the band gap (0 extra e^-) leading to a steep decline with increasing electron doping. As can be seen, the EFG evolution with electron doping is solely given by the lowest conduction band.

Surprisingly, the evolution of the EFG in Bi_2Se_3 upon doping in the SOC case shows *not* a reversed NoSOC behavior. That is, one might have expected that a steep dependence is

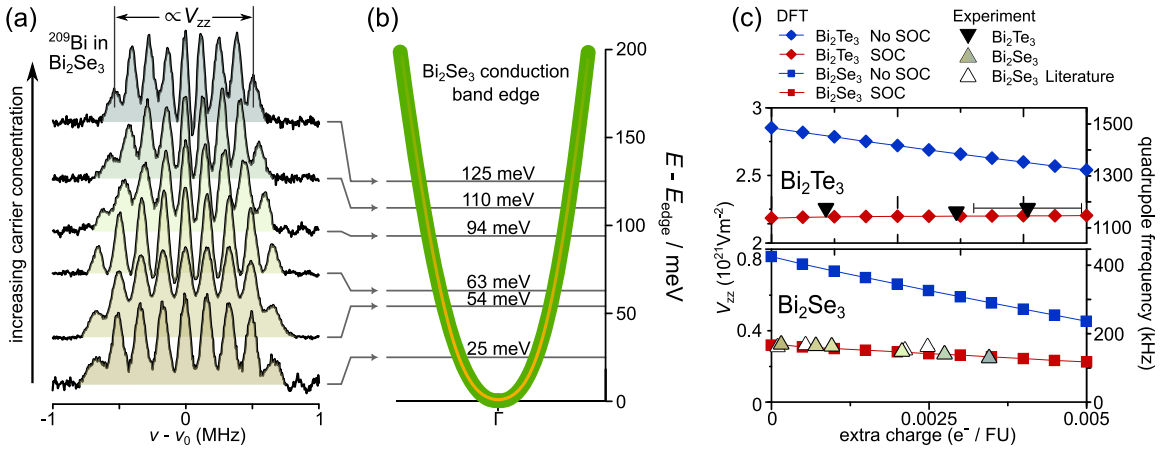

FIG. 4. (a) ^{209}Bi quadrupole spectra at 11.74 T room temperature with the quadrupole splitting proportional to V_{ZZ}. With increasing carrier concentration, the splitting reduces measurably. In panel (b), the corresponding shift of the Fermi level into the conduction band is illustrated. (c) Calculated V_{ZZ} for Bi_2Se_3 and Bi_2Te_3 without (blue) and with (red) SOC (band inversion). The experimental data points (triangles) agree well with the calculations when SOC is enabled and thus, band inversion emerges.

observed for the hole doping because of the band inversion preoccupying Bi states, and a weak dependence upon electron doping. Rather, the EFG decreases monotonically across the whole doping range without any visible discontinuity at the band gap. The corresponding occupations in Fig. 3, panel (a), provide an explanation. Once SOC is switched on, the p_z states of Bi and Se_{out} *and* the Bi $p_{x/y}$ are continuously populated throughout the regarded doping range. This suggests, that due to SOC the order of Bi and Se p_z is not just inverted, but rather, the states are evenly distributed in the considered energy range, and on top of that, Bi $p_{x/y}$ states are mixed in. In this sense, the band inversion is part of a mixture of states closest to the Fermi level, and thus, has no edges in the k space neither toward $\pm k$, nor toward the band gap.

The situation in Bi_2Te_3 is different. Both the populations [Fig. 3(d)] as well as the EFG [Fig. 3(e)] show a slight bend at 0 extra electrons even in the case of SOC. However, similar to Bi_2Se_3, the slopes of the EFG for hole and electron doping do not reverse upon enabling SOC. Again, the simple picture of an exchange in terms of a discrete band inversion is not observed. It has to be noted, though, that the direct band gap at the Γ point for NoSOC changes to an indirect gap in the vicinity of the Z point with SOC, as can be seen in Fig. 3(f). Nevertheless, the inverted and mixed band structure is still accessible with doping (cf. pink solid lines). For the conduction band, the large contribution from Te_{out} states and the uniform increase of Bi p_z and $p_{x/y}$ states leave the EFG to be almost independent of electron doping.

The DFT calculations as provided in Figs. 2 and 3 give a clear account of the changes in the band structure of Bi_2Se_3 and Bi_2Te_3 introduced by SOC, including the topological band inversion, and how much of that is reflected in the real-space EFG. It follows that the measurement of the EFG in an undoped sample allows no statement about the presence of a band inversion due to the large contributions from deeper states. Real samples of Bi_2Se_3 and Bi_2Te_3 feature a strong chemical tendency for self-doping, creating numerous native defects such as vacancies or antisites. This yields the typical low bulk resistivity which has always been a critical drawback of these materials as it hampers the characterization of the surface states [17,18]. In the current case of exploring the bulk band structure, however, doping is advantageous because it allows to explore the Fermi edge with the Fermi level shifted progressively into the conduction (valence) band with increasing electron (hole) doping.

The comparison between experimental results of the local Bi EFG in Bi_2Se_3 and Bi_2Te_3 for various doping levels and with DFT is shown in Fig. 4. To obtain V_{ZZ} from the experiment, we assume a first-order approximation of the quadrupole interaction, typically written as

$$\mathcal{H}_Q = \frac{3I_z^2 - I(I+1)}{4I(2I-1)} eQ \times V_{ZZ} \times \mathcal{F}(\beta, \alpha, \eta), \qquad (1)$$

where eQ denotes the electric nuclear quadrupole moment and $\mathcal{F}(\beta, \alpha, \eta)$ contains the interaction anisotropy which depends on the relative orientation (Euler angles α and β) of the EFG with respect to the external field, as well as on the asymmetry factor $\eta = (V_{XX} - V_{YY})/V_{ZZ}$ that relates the diagonal elements of the traceless EFG in its principle axes system (PAS). In agreement with DFT calculations, the EFG tensor for Bi nuclei in Bi_2Se_3 and Bi_2Te_3 has been determined to be axially symmetric ($\eta = 0$) and aligned with the crystal c axis [13,19,20]. Thus, for single-crystal NMR measurements at $c \parallel B_0$, the quadrupole splitting ν_Q translates into the EFG as

$$\nu_Q = \frac{3eQV_{ZZ}}{2I(2I-1)h}. \qquad (2)$$

In panel (a) of Fig. 4, Bi quadrupole patterns obtained from various Bi_2Se_3 single crystals for $c \parallel B_0$ are shown. The spectra were obtained at room temperature and 11.74 T using broad band measurements (see methods for details). To extract the quadrupole splitting frequency ν_Q, a set of nine equidistant Gaussians with appropriate relative intensities were used to fit the spectra.

Visibly, with increasing electron doping (from bottom to top), the line splitting reduces, confirming the sensibility of the EQI for additional charge carriers. In Fig. 4, panel (b), the

conduction band edge is sketched with the arrows indicating the shift of the Fermi level into the conduction band with increasing electron doping (up to 125 meV for 2×10^{19} cm^{-3}). ^{209}Bi spectra of Bi_2Te_3 feature a much larger and an essentially carrier-independent line splitting, and can be found in earlier publications [19,20]. For both materials, the carrier-dependent EQI convincingly reproduces the doping evolution of V_{ZZ} for the band inversion case [Fig. 4(c), red symbols], while the trivial band structure would feature a much steeper dependence. It has to be noted, though, that there is a certain degree of freedom (of about 15%) in the calculations in terms of the absolute values of V_{ZZ} depending on the used lattice parameters, e.g., it matters whether DFT-optimized crystal structure is used, or experimentally measured ones. This, however, does not affect the slope of $V_{ZZ}(n)$.

III. CONCLUSIONS

In summary the real-space charge redistribution induced by SOC and the band inversion in the topological insulator Bi_2Se_3 and Bi_2Te_3 is studied with DFT and NMR. SOC has a significant effect on the electronic states deep in the valence band and mixes the states around the Fermi level. This includes Bi and Se_{out} p_z states (much less so Se_{in}), which gives rise to the topologically nontrivial band inversion. However, this nontrivial band inversion is embedded in a homogeneous mixing of states across the band gap for a broad range of doping, that also heavily involves Bi $p_{x/y}$ states. In other words, the valence and conduction band Fermi edge have the same mixed character and the topological band inversion has no edges in the k space, neither towards the valence (conduction) band, nor at the band gap. Using the electric quadrupole interaction of ^{209}Bi nuclei, the charge redistribution can be studied systematically in doped single crystals. The work shows that a combination of DFT and a real-space method like NMR can provide crucial insight even into k-space properties of complex topological matter and might be utilized in future studies of related phenomena.

IV. METHODS

Electronic structure was studied using the all-electron full-potential code WIEN2k [21] within the framework of DFT. The atomic sphere radii were chosen as 2.65 a_0 for Bi and 2.30 a_0 for Se (1 bohr, $a_0 = 5.29 \times 10^{-11}$ m). The basis set consisted of approximately 1240 functions ($R_{MT} \times K_{max} = 9.5$), the reciprocal space was sampled using 891 k points ($21 \times 21 \times 21$ mesh). Perdew-Burke-Ernzenhof (PBE) variant [22] of the generalized gradient approximation (GGA) was adopted to approximate the exchange-correlation potential, using a fine FFT mesh ($405 \times 405 \times 405$) in the interstitial region. The lattice parameters of the rhombohedral unit cell and the positions of Bi and Se atoms were fully optimized, including the dispersion energy due to the van der Waals (VdW) interaction as implemented in WIEN2k [23]. For VdW calculation, the cutoff for the Fourier expansion of the charge density was enhanced to 20 a_0^{-1}. All relevant parameters were properly converged with respect to the atomic forces and values of the electric-field gradient of Bi.

Where enabled, the spin-orbit coupling was included within the second variational method using the scalar-relativistic approximation [24]. For the density of states (DOS) plots, the number of k points was increased to 5340 ($39 \times 39 \times 39$ mesh). All terms of the electric field gradient tensor were calculated, the decomposition of EFG onto the contributions of individual bands in the DOS plot was done by selecting the corresponding energy ranges. The charge-carrier density was modeled by adding/removing valence charge, the charge neutrality of the unit cell was maintained by compensating such an extra charge with a homogeneously charged background. For the band-structure plots the basis set was enhanced to 1656 functions ($R_{MT} \times K_{max} = 10.5$). Charge density of the unit cell was plotted on a grid of $200 \times 200 \times 200$ points using VESTA program [25].

The synthesis and characterization of Bi_2Se_3 and Bi_2Te_3 samples as investigated in this work, including two additional single crystals of Bi_2Se_3, i.e., $Bi_{1.85}Se_3$ and $Bi_{1.90}Se_3$, are documented elsewhere [13,19,20,26,27]. The spectra shown in Fig. 4(a) were obtained at 11.74 T and room temperature using broad-band solid echo measurements ($\pi/2$ pulse width of 0.6 µs) in combination with low quality factors ($Q \approx 20$). The pulse separation times were adjusted to $2/\nu_Q$ (between 12 and 15 µs) for each sample to optimize the outcome due to the interplay of hardware dead times (~5 µs), echo widths (12 to 15 µs), and very short $T_2 \approx 15$ µs. Short spin-lattice relaxation times ($T_1 \sim 15$ ms) allow for rapid signal averaging while the usage of rather small rf coils (~$3 \times 3 \times 1$ mm^3) with filling factors close to 1 prevents heating of the sample. Due to the much larger quadrupole splitting for Bi in Bi_2Te_3, selective spin echoes were used to measure individual resonances [13,19,20].

ACKNOWLEDGMENTS

The authors thank J. Haase and I. Garate for fruitful discussions. R.G. also thanks B. Fine and J. Nachtigal. Computational resources were provided by the e-INFRA CZ project (ID:90254), supported by the Ministry of Education, Youth and Sports of the Czech Republic.

[1] B. J. Wieder, B. Bradlyn, J. Cano, Z. Wang, M. G. Vergniory, L. Elcoro, A. A. Soluyanov, C. Felser, T. Neupert, N. Regnault, and B. A. Bernevig, Topological materials discovery from crystal symmetry, Nat. Rev. Mater. **7**, 196 (2022).

[2] L. M. Nash, D. Kleckner, A. Read, V. Vitelli, A. M. Turner, and W. T. M. Irvine, Topological mechanics of gyroscopic metamaterials, Proc. Natl. Acad. Sci. USA **112**, 14495 (2015).

[3] L. M. Schoop, F. Pielnhofer, and B. V. Lotsch, Chemical principles of topological semimetals, Chem. Mater. **30**, 3155 (2018).

[4] H. Zhang, C.-X. Liu, X.-L. Qi, X. Dai, Z. Fang, and S.-C. Zhang, Topological insulators in Bi_2Se_3, Bi_2Te_3 and Sb_2Te_3 with a single Dirac cone on the surface, Nat. Phys. **5**, 438 (2009).

[5] Y. Xia, D. Qian, D. Hsieh, L. Wray, A. Pal, H. Lin, A. Bansil, D. Grauer, Y. S. Hor, R. J. Cava, and M. Z. Hasan, Observation of a large-gap topological-insulator class with a single Dirac cone on the surface, Nat. Phys. **5**, 398 (2009).

[6] Y. L. Chen, J. G. Analytis, J.-H. Chu, Z. K. Liu, S.-K. Mo, X. L. Qi, H. J. Zhang, D. H. Lu, X. Dai, Z. Fang, S. C. Zhang, I. R. Fisher, Z. Hussain, and Z.-X. Shen, Experimental realization of a three-dimensional topological insulator, Bi_2Te_3, Science **325**, 178 (2009).

[7] H. Yasuoka, T. Kubo, Y. Kishimoto, D. Kasinathan, M. Schmidt, B. Yan, Y. Zhang, H. Tou, C. Felser, A. P. Mackenzie, and M. Baenitz, Emergent Weyl fermion excitations in TaP explored by ^{181}Ta quadrupole resonance, Phys. Rev. Lett. **118**, 236403 (2017).

[8] Y. Tian, N. Ghassemi, and J. H. Ross, Dirac electron behavior and NMR evidence for topological band inversion in $ZrTe_5$, Phys. Rev. B **100**, 165149 (2019).

[9] W. Papawassiliou, A. Jaworski, A. J. Pell, J. H. Jang, Y. Kim, S.-C. Lee, H. J. Kim, Y. Alwahedi, S. Alhassan, A. Subrati, M. Fardis, M. Karagianni, N. Panopoulos, J. Dolinšek, and G. Papavassiliou, Resolving Dirac electrons with broadband high-resolution NMR, Nat. Commun. **11**, 1285 (2020).

[10] C. G. Wang, Y. Honjo, L. X. Zhao, G. F. Chen, K. Matano, R. Zhou, and G.-Q. Zheng, Landau diamagnetism and Weyl-fermion excitations in TaAs revealed by ^{75}As NMR and NQR, Phys. Rev. B **101**, 241110(R) (2020).

[11] D. Tay, T. Shang, P. Puphal, E. Pomjakushina, H.-R. Ott, and T. Shiroka, Unusual ^{27}Al NMR shift in the Weyl-fermion systems LaAlGe and PrAlGe, Phys. Rev. B **102**, 241109(R) (2020).

[12] Y. Tian, Y. Zhu, R. Li, Z. Mao, and J. H. Ross, NMR determination of Van Hove singularity and Lifshitz transitions in the nodal-line semimetal ZrSiTe, Phys. Rev. B **104**, L041105 (2021).

[13] R. Guehne, V. Chlan, G. V. Williams, S. V. Chong, K. Kadowaki, A. Pöppl, and J. Haase, Unusual ^{209}Bi NMR quadrupole effects in topological insulator Bi_2Se_3, J. Magn. Reson. **302**, 34 (2019).

[14] A. Isaeva and M. Ruck, Crystal chemistry and bonding patterns of bismuth-based topological insulators, Inorg. Chem. **59**, 3437 (2020).

[15] K. Schwarz, C. Ambrosch-Draxl, and P. Blaha, Charge distribution and electric-field gradients in $YBa_2Cu_3O_{7-x}$, Phys. Rev. B **42**, 2051 (1990).

[16] P. Blaha, K. Schwarz, and P. H. Dederichs, First-principles calculation of the electric-field gradient in hcp metals, Phys. Rev. B **37**, 2792 (1988).

[17] R. J. Cava, H. Ji, M. K. Fuccillo, Q. D. Gibson, and Y. S. Hor, Crystal structure and chemistry of topological insulators, J. Mater. Chem. C **1**, 3176 (2013).

[18] B. Skinner, T. Chen, and B. I. Shklovskii, Why is the bulk resistivity of topological insulators so small? Phys. Rev. Lett. **109**, 176801 (2012).

[19] R. Guehne, J. Haase, C. Shekhar, and C. Felser, Field-induced charge symmetry revealed by nuclear magnetic resonance in the topological insulator Bi_2Te_3, Phys. Rev. Res. **3**, L012018 (2021).

[20] R. Guehne, G. V. M. Williams, S. V. Chong, and J. Haase, Unusual quadrupole NMR of topological insulator Bi_2Te_3, J. Phys. Chem. C **125**, 6743 (2021).

[21] P. Blaha, K. Schwarz, F. Tran, R. Laskowski, G. K. H. Madsen, and L. D. Marks, Wien2k: An APW + lo program for calculating the properties of solids, J. Chem. Phys. **152**, 074101 (2020).

[22] J. P. Perdew, K. Burke, and M. Ernzerhof, Generalized gradient approximation made simple, Phys. Rev. Lett. **77**, 3865 (1996).

[23] F. Tran, J. Stelzl, D. Koller, T. Ruh, and P. Blaha, Simple way to apply nonlocal van der Waals functionals within all-electron methods, Phys. Rev. B **96**, 054103 (2017).

[24] A. H. MacDonald, W. E. Picket, and D. D. Koelling, A linearised relativistic augmented-plane-wave method utilising approximate pure spin basis functions, J. Phys. C Solid State **13**, 2675 (1980).

[25] K. Momma and F. Izumi, *VESTA3* for three-dimensional visualization of crystal, volumetric and morphology data, J. Appl. Crystallogr. **44**, 1272 (2011).

[26] N. M. Georgieva, D. Rybicki, R. Guehne, G. V. M. Williams, S. V. Chong, K. Kadowaki, I. Garate, and J. Haase, ^{77}Se nuclear magnetic resonance of topological insulator Bi_2Se_3, Phys. Rev. B **93**, 195120 (2016).

[27] B. Mallett, S. Chong, R. Guehne, A. Chan, P. Murmu, J. Kennedy, and R. Buckley, The electronic properties and defect chemistry of $Bi_{2-x}Se_3$, $-0.05 < x < 0.15$, J. Phys. Chem. Solids **148**, 109752 (2021).